Coastal Engineering 128 (2017) 37–43

Contents lists available at ScienceDirect

Coastal Engineering

journal homepage: www.elsevier.com/locate/coastaleng

Short communication

# High-resolution monitoring of wave transformation in the surf zone using a LiDAR scanner array

Kévin Martins [a], Chris E. Blenkinsopp [a,*], Hannah E. Power [b], Brittany Bruder [c], Jack A. Puleo [c], Erwin W.J. Bergsma [a]

[a] Research Unit for Water, Environment and Infrastructure Resilience (WEIR), University of Bath, UK
[b] University of Newcastle, Australia
[c] University of Delaware, USA

ARTICLE INFO

*Keywords:*
Surf zone
Breaking waves
Terrestrial laser scanners (LiDAR)
Wave-by-wave approach

ABSTRACT

Understanding of breaking and broken waves is key for the prediction of nearshore sediment transport and coastal hazards, however the difficulty of obtaining measurements of highly unsteady nearshore waves has limited the availability of field data. This paper reports on a novel field experiment designed to capture the time-varying free-surface throughout the surf and swash zones was conducted on a dissipative sandy beach using an array of 2D LiDAR scanners. Three scanners were deployed from the pier at Saltburn-by-the-Sea, UK for a 6 day period to monitor the surface elevation of nearshore waves from the break point to the runup limit at temporal and spatial resolutions (order of centimetres) rarely achieved in field conditions. The experimental setup and the procedure to obtain a continuous time series of surface elevation and wave geometry is described. A new method to accurately determine the break point location is presented and compared to existing methodologies.

## 1. Introduction

The surf zone is the most energetic area of the nearshore, characterised by the presence of breaking and broken waves. Depth-induced wave breaking is a complex physical process, which leads to dissipation of energy through a variety of processes including the injection of air (*e.g.* Blenkinsopp and Chaplin, 2007) and turbulence (*e.g.* Longo (Longo et al., 2002)) into the water column as well as the generation of splashes and noise (Carey and Fitzgerald, 1993).

Due to the difficulty of obtaining high quality data in the energetic surf zone, existing field data are primarily from major field experiments: for example DUCK (Ebersole and Hughes, 1987), DELILAH (Birkemeier et al., 1997) and SUPERDUCK (Rosati et al., 1990) in the USA and more recently in Europe with the ECORS experiments (Senechal et al., 2011). Although the coastal community's knowledge of nearshore processes and wave transformation has greatly benefited from these experiments, they were generally limited by the cross-shore resolution of the measurements. Wave breaking involves a rapid transformation of wave geometry, and the break point constantly moves over time due to changing wave conditions and variation of mean water levels. The deployment of *in-situ* instruments such as photopoles, pressure transducers or wave gauges can therefore only bring limited insight into the rapid changes in shape that a wave undergoes around the break point. As well as being non intrusive, remote sensors can generally cover larger scale with a better spatial resolution (*e.g.* RaDAR or video imaging, Holman and Haller (2013)) and can easily be deployed and maintained at the coast. However, most remote sensors are not capable of directly measuring the wave geometry.

Recent studies have demonstrated the ability of LiDAR scanners to obtain accurate measurements of the water surface and depth-averaged velocity at hundreds of points within the swash zone of a sandy beach (Blenkinsopp et al., 2012), and also the morphodynamics of gravel beaches (Almeida et al., 2015). In deeper water, the study of waves propagating in the inner surf zone of a dissipative sandy beach was made possible by deploying a tower-mounted LiDAR scanner close to the shoreline (Martins et al., 2016) or on a dune (Brodie et al., 2015). Brodie et al. (2015) demonstrate the potential of LiDAR scanners to monitor inner surf zone waves with high spatial extent and resolution by comparing the estimated spectral and third moment wave properties to pressure transducer data. More recently, Martins et al. (2017) show that it is possible with a LiDAR scanner to accurately capture the shape of individual breaking waves (wave height, skewness and asymmetry), underlining significant differences between pressure-derived surface

* Corresponding author.
*E-mail address:* c.blenkinsopp@bath.ac.uk (C.E. Blenkinsopp).

http://dx.doi.org/10.1016/j.coastaleng.2017.07.007
Received 25 January 2017; Received in revised form 26 July 2017; Accepted 28 July 2017

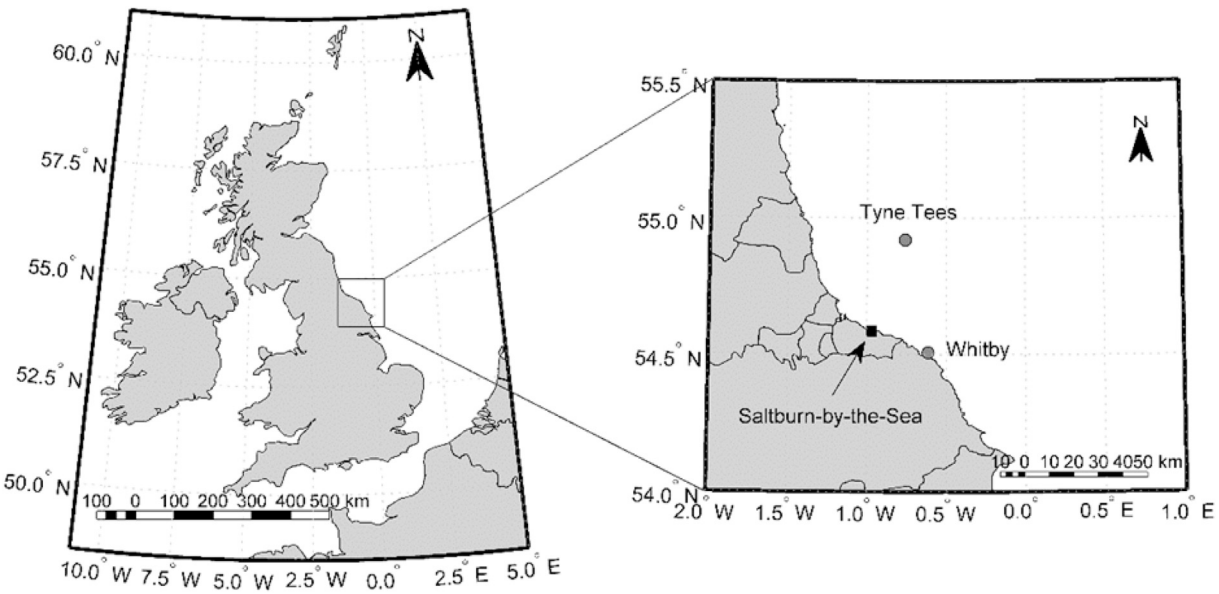


**Fig. 1.** Map of the UK, zoomed around the field site area. The location of Saltburn-by-the-Sea is shown as the black square in the zoomed map, while the nearshore (Whiby) and offshore (Tyne Tees) buoys are shown as the grey dots. This part of the coastline is oriented to 18°NE in the North Sea.

elevation and the scanner dataset.

Accurate detection of the break point is desired because it defines the seaward limit of the surf zone, where the behaviour of propagating waves changes significantly from a progressive surface wave to a bore, characterised by high levels of aeration and energy dissipation (Svendsen et al., 1978). Methods to define the break point based on wave geometry obtained from *in-situ* gauges (*e.g.* Stokes limiting steepness of $H/L < 1/7$) or surface elevation vertical velocity $\partial\eta/\partial t$ have been used in deep water (Babanin, 2011). In shallower waters where spatial resolution is key, other methods mostly based on remote-sensing techniques (video methods (Haller and Catalán, 2009), infrared imagery (Carini et al., 2015), and microwave backscattering from breakers (Catalán et al., 2014)) have been used. Here, a new method to extract the break point from the high-resolution LiDAR dataset is discussed and compared to other commonly used criteria.

## 2. Methodology

### 2.1. Field site and wave conditions

A field experiment was undertaken between 7th April and 13th April 2016 at Saltburn-by-the-Sea, on the North East coast of England (Fig. 1).

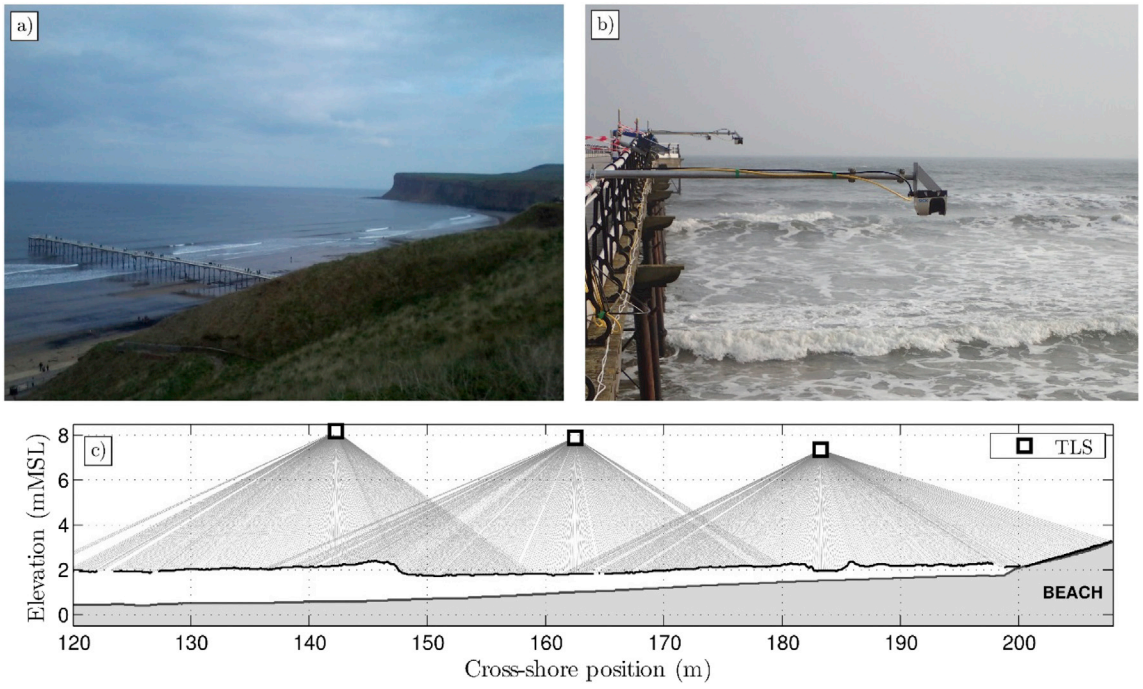


**Fig. 2.** Field site and LiDAR scanners deployment. Panel a) shows the Saltburn beach pier, protected from the Eastern seas by a cliff. Panel b) shows the LiDAR scanners deployment: deployed in the first third of the pier, the scanners were deployed 2.5 m away from the pier, using a 'T' shaped scaffolding system relying on the pier railing system. Panel c) shows a schematic of the set-up with an example of post-processed free surface elevation (black thick line while individual measurements are shown as light grey lines). The beach profile (thick grey line) corresponds to the surveyed profile during the previous low tide.

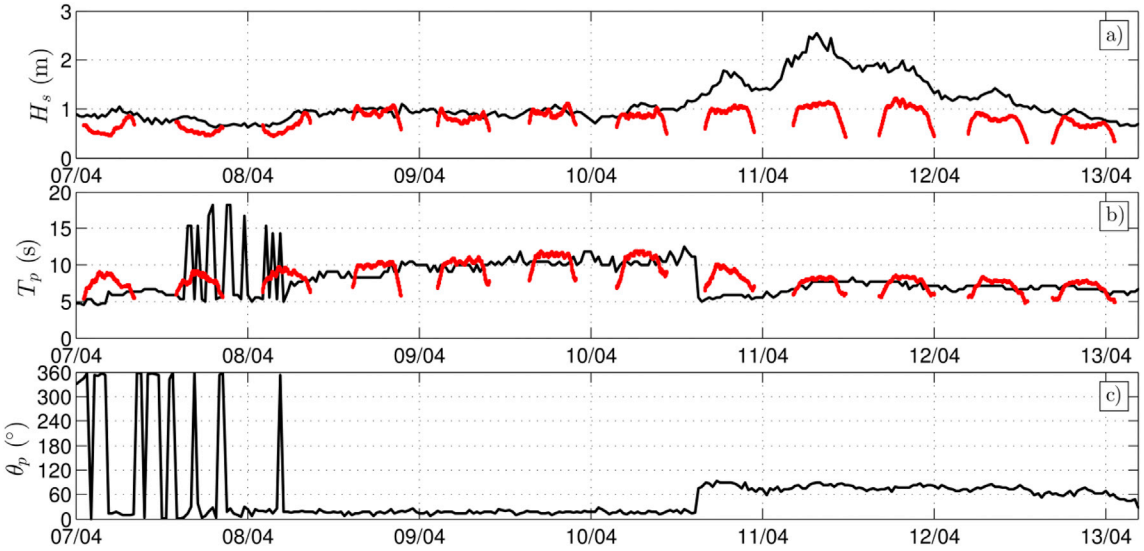


**Fig. 3.** Nearshore wave conditions during the field experiment: a) Significant wave height $H_s$, b) Peak period $T_p$ and c) Peak direction $\theta_p$. In every panel measured conditions at Whitby buoy (courtesy of http://www.channelcoast.org/) are shown as black lines, while the conditions measured at the seaward edge of the pier by the pressure transducer are shown as red lines (only $H_s$ and $T_p$). (For interpretation of the references to colour in this figure legend, the reader is referred to the web version of this article.)

The beach at Saltburn is home to a 206 m long pier which was used to facilitate the experimental methodology described below (Fig. 2). This part of the UK coastline is macrotidal: the measured tidal range at the harbour at Whitby reached a maximum of 5.42 m on 08/04 decreasing to 3.47 m on 13/04. The beach at Saltburn consists of a wide, sandy low gradient intertidal beach ($\tan\beta\tilde{}1:65$) backed by a steeper cobble slope ($\tan\beta\tilde{}1:6$). Between low and mid-tide, conditions are dissipative whereas when the mean water level reaches the lower part of the cobble slope, conditions become more reflective. The measurements described below focused on the period from mid to high tide and thus captured both dissipative and reflective conditions.

The wave climate at Saltburn is bi-modal with a combination of Northerly swell and Easterly wind-sea waves: deepwater average wave peak period ( $T_p$) measured at the Tyne Tees Waverider buoy in 65 m water depth (see Fig. 1 for the buoy location) are 9.4 s and 6.2 s respectively for these two direction quadrants. Fig. 3 shows the nearshore wave conditions during the experiment measured by the Whitby Waverider buoy (17 m depth, see Fig. 1 for the buoy location) and by a pressure transducer installed at the offshore limit of the pier. Throughout the course of the experiments, the significant wave height $H_s$ at the end of the pier remained relatively constant around 1 m (Fig. 3a). However, wave direction and period changed abruptly on 11/04, when Easterly wind seas became predominant over the Northerly swell (Fig. 3b–c).

### 2.2. Experimental setup

Three SICK LMS511 commercial 2D LiDAR scanners were cantilevered over the side of the pier on braced scaffold poles extending 2.5 m from the safety railing (Fig. 2b). The LiDAR scanners were positioned 20 m apart along the pier and at a height from the sand surface ranging from 5.9 m to 7.6 m, which enabled measurements of the free-surface data along an approximately 100 m long cross-shore transect, depending on surf zone width. Data were recorded continuously during each mid-high-mid tide cycle at a frequency of 25 Hz and an angular resolution of 0.1667°. Fig. 2c displays the cross shore profile of the experimental set up, along with an example of the LiDAR measurements.

The LiDAR scanners were positioned on the East side of the pier such that the majority of wave rays did not pass beneath the pier before reaching the LiDAR scanning profile. Optimal conditions for the study of the cross-shore transformation of surf zone waves occurred during Northerly swell conditions (09/04 and 10/04) when after refraction, incoming waves propagate parallel to the pier (oriented to 18°NE in the North Sea). Additionally, by deploying the scanners 2.5 m from the pier structure, the influence of splashes from the pier legs was minimised, though in fact, due to the relatively small diameter of the pier legs, little splashing was observed.

In addition to the LiDAR scanners, one RBR pressure transducer (PT) was deployed at $x = 16$ m, and sampled at 2 Hz ($x = 0$ m taken as the offshore limit of the pier, and $x$ is positive towards shore). Finally, beach profiles were measured using a total station and RTK GPS at every low tide.

### 2.3. Processing of the lidar data

As demonstrated by Blenkinsopp et al. (2012, 2010), successful detection of an air-water interface by LiDAR requires the presence of foam or bubbles at the surface. Each LiDAR scanner consistently detected the free-surface at hundreds of locations along a cross-shore transect spanning 40–50 m. The spatial resolution varied with distance from the LiDAR but was generally 0.02 m beneath the scanner and up to 0.25 m at the outer edges of each LiDAR scan (see Fig. 2c).

A combined dataset of surface elevation comprising the three individual LiDAR datasets was used to track waves across the surf zone. The location of each scanner was first surveyed using a total station. After geo-location, each of the individual LiDAR scanner datasets underwent a series of transformations (see Martins et al. (2016). for further detail): roll angle correction using surveys of beach profile, despiking and spatial interpolation into a 0.1-m regular cross-shore grid. This series of steps provides a time-series of water surface profiles for each of the three scanners as indicated in Fig. 2c. A linear weighting function was used in the regions where there was overlapping LiDAR data ($x = 142$-$162$ m and $x = 162$-$182$ m) to prioritise the data with a smaller angle of incidence with the free surface. At any position where the data from one of the instruments was invalid, for example when the line-of-sight to a wave trough was obscured by the wave crest, the measurement from the other scanner only was used.

The differences observed between the LiDAR measurements in the overlapping areas have been quantified in terms of Root-Mean Square Errors (*RMSE*) between individual LiDAR datasets. Consistency between adjacent instruments was observed throughout the experiment, with the largest average *RMSE* over an overlap region being 0.037 m, which is just four times the order of magnitude of the noise observed from a single

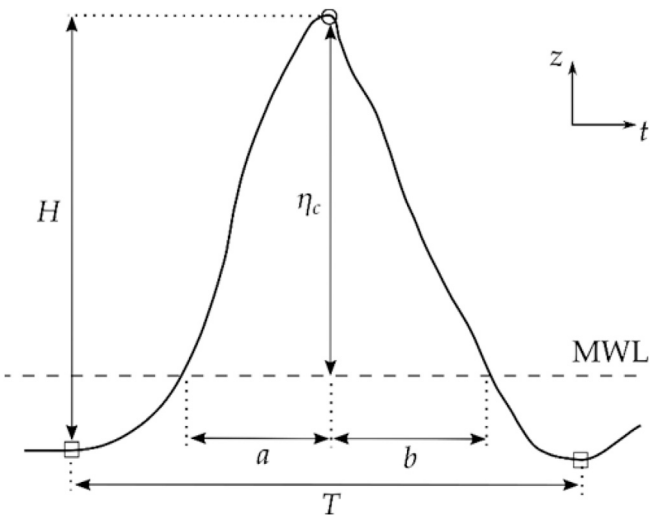


**Fig. 4.** Nomenclature adopted for the definition of spatial and temporal individual wave parameters: based on Mean Water Level (MWL), $\eta_c$ defines the crest height elevation above MWL, $H$ the distance between wave crest and preceding trough. The parameters $a$ and $b$ represent the time elapsed for the surface elevation to reach the crest elevation from up-crossing MWL and the time elapsed for the surface elevation to down-cross MWL from the crest elevation. The squares represent the two surrounding troughs, defining the individual wave period of the wave. The crest is designated by a circle.

sensor measuring a dry surface (Martins et al., 2016), and comparable to the local variation of the water surface due to 3D effects and splashes. Although lower standard deviations over the overlap regions was observed for swell conditions (09/04 and 10/04), no clear trend of the observed *RMSE* between instrument datasets with the wave conditions (Fig. 3) was found.

## 3. Detection of the break point

Identifying the break point location in any free surface dataset is difficult due to the rapid and relatively limited spatial extent of the breaking process. A new method (hereafter referred to as gradient variance method; GVM) is described in 3.2. GVM uses the high-resolution dataset obtained from the LiDAR scanners to detect the evolution of small features in the broken wave front. The ability of GVM to detect the break point was compared to a range of other break point criteria for a dataset of 116 waves:

- location of maximum wave height $H$ (Svendsen et al., 1976),
- location where the rate of change of surface elevation $\partial\eta/\partial t$ exceeds a threshold (equivalent to the rate of rise in (Longuet-Higgins and Smith, 1983)),
- location of maximum wave skewness $S_k$ (Svendsen, 2006),
- location of minimum wave asymmetry $A_t$ (Svendsen, 2006).

$H$ and the rate of change of surface elevation should reach their maximum at break point, because the wave steepness reaches its maximum at the break point location. Similarly, the wave skewness should reach its maximum while the asymmetry decreases significantly at the break point.

The ground truth method consists of the visual assessment of the break point from measured wave profile animations. The break point was visually estimated for each individual wave at the crest location when one of the following signs was apparent (Cowell, 1982): spray at the wave crest, wave front close to the wave crest about to overturn (vertical) and/or a disturbance or high frequency peaks in the wave front (suggesting a spilling-type of breaker). As the ground truth method is subjective to the user, the same analysis was performed by four people on a reduced subset of 41 waves. The *RMSE* between the user's datasets had minimum (maximum) values of 1.5 m (2.6 m), with corresponding standard deviation values of 1.4 m (2.2 m).

### 3.1. Wave-by-wave approach

To detect the break point, GVM relies on a previously developed wave-by-wave approach that involves tracking individual waves from the shoaling region and through the surf zone (Martins et al., 2016, 2017). In this wave-by-wave approach, wave crests were identified by detecting peaks in the surface elevation timeseries at each cross-shore grid location. Starting at an initial cross-shore location, the wave crests were then tracked through the surf zone and at each cross-shore location, and the following individual wave properties were extracted: individual wave height $H$, wave period $T$ and trough levels $h_t$, along with spatial (eq. (1)) and temporal (eq. (2)) definitions of wave asymmetry:

$$A_s = \eta_c/H \tag{1}$$

$$A_t = a/b \tag{2}$$

where the parameters in equations (1) and (2) are defined in Fig. 4 (Adeyemo, 1968). The vertical spatial asymmetry was used to define the individual wave skewness:

$$S_k = A_s - 0.5. \tag{3}$$

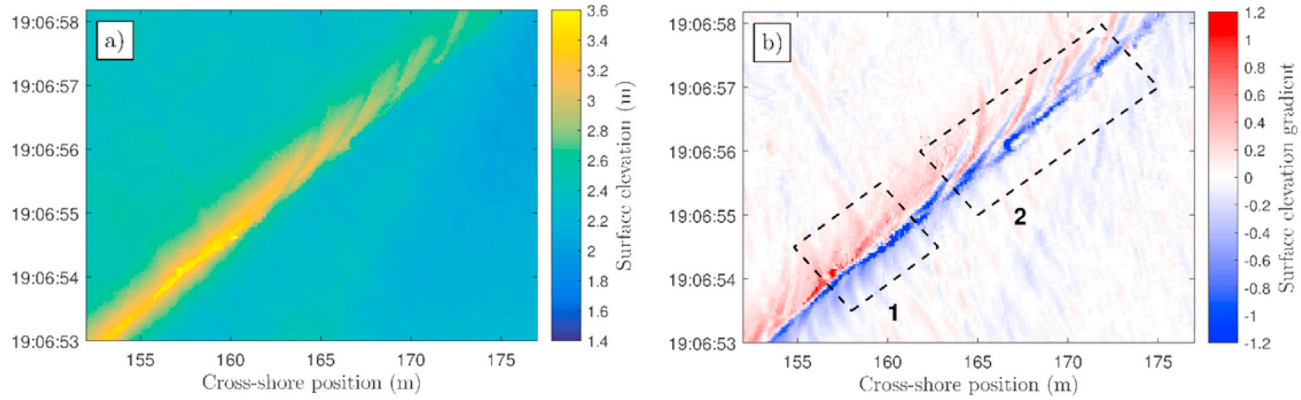


**Fig. 5.** Example of surface elevation timestack of a breaking wave: a) shows the surface elevation in the Saltburn Mean Sea Level (MSL) datum, while b) shows the corresponding spatial surface elevation gradient $\partial\eta/\partial x$. The two dashed rectangles in panel b) represent the two distinct phases during the breaking process: 1 corresponds to the breaking onset, with the maximum wave height and minimum gradient in front of the wave reached; 2 corresponds to the early stage of propagation as a bore. (For interpretation of the references to colour in this figure legend, the reader is referred to the web version of this article.)

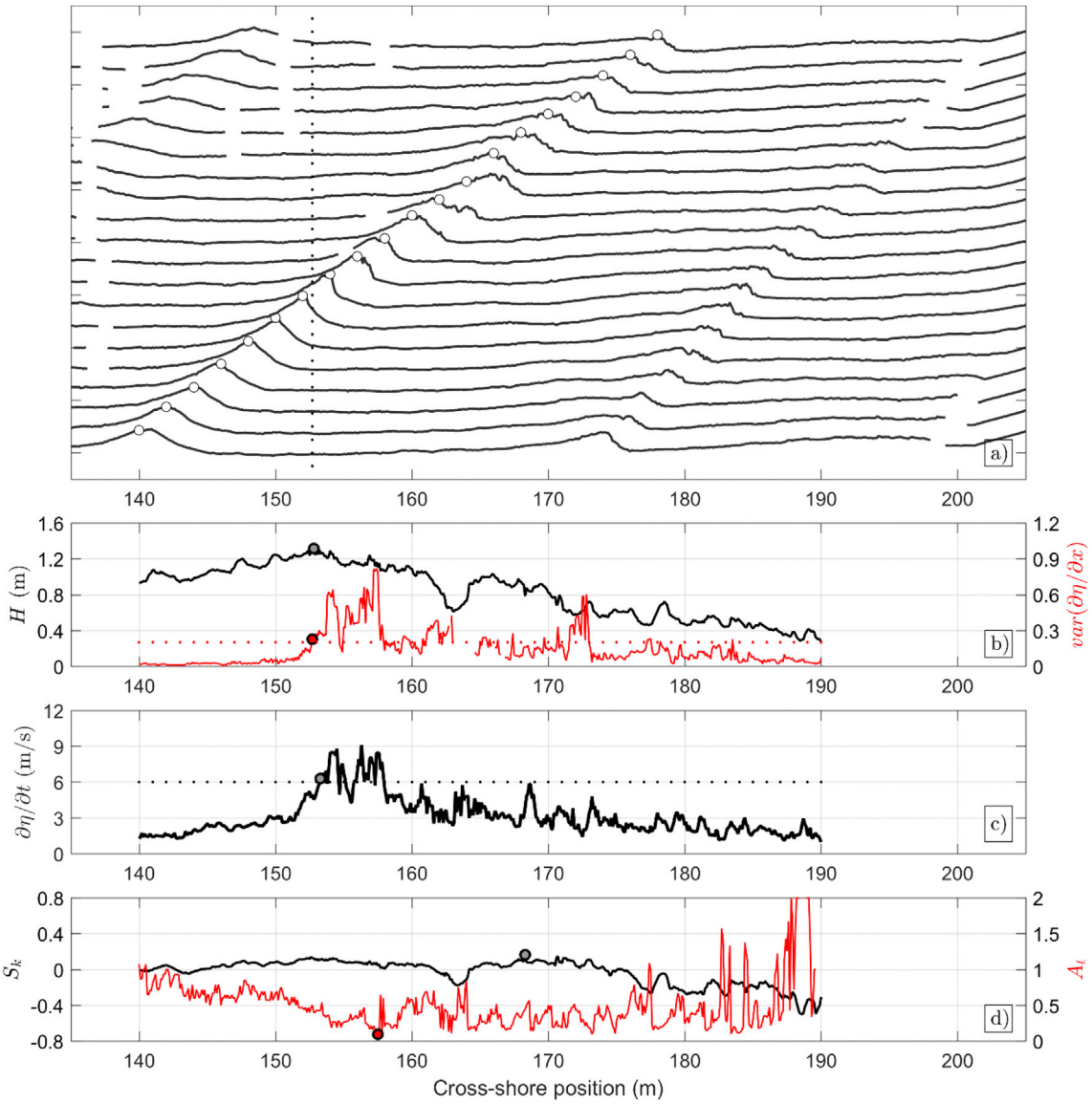


**Fig. 6.** Propagation of a breaking wave on 09/04. Panel a) shows the wave profile evolution through the surf zone: a complete profile is shown at the time when the maximum water surface elevation (wave crest) is detected at 2 m cross-shore increments. The break point location is shown as vertical dotted line. Panel b) shows the cross-shore evolution of the individual wave height $\boldsymbol{H}$ (black line), shown with the variance of the surface elevation gradient in front of the wave (red line). The red dotted threshold line of 0.2 is also shown. The break points are shown as grey and red dot for the $\boldsymbol{H}$-based method and GVM respectively. Panel c) shows the maximal surface elevation rate of change in front of the wave. The threshold line used for this method (6 m/s) is shown as dotted black line Panel d) shows the individual wave skewness ($\boldsymbol{S_k}$) and wave time asymmetry ($\boldsymbol{A_t}$) as black and red lines respectively. The break points are shown as grey and red dot for the $\boldsymbol{S_k}$-based and $\boldsymbol{A_t}$-based methods respectively. (For interpretation of the references to colour in this figure legend, the reader is referred to the web version of this article.)

which has a value close to zero when the wave profile is centered on the Mean Water Level (MWL). In the analysis described here, wave periods are defined by the time elapsed between the passages of the two troughs surrounding the wave crests at a same location (Fig. 4).

### 3.2. Break point detection using the gradient variance method

The principle of GVM to detect the break point takes advantage of the ability of the LiDAR to capture small-scale features in the broken wave front. Fig. 5 shows timestack examples of surface elevation and surface elevation spatial gradient (based on central differences) of a breaking wave from 10/04. Prior to the break point ($x = 158$ m), the surface elevation around the crest of the shoaling wave is smooth (Fig. 5a) and the corresponding spatial gradients in front and behind the wave crest are relatively constant, and respectively negative and positive (Fig. 5b). At the onset of breaking, the surface elevation reaches its maximum (Fig. 5a), and the maximum absolute gradient is reached at the wave front face (phase 1 in Fig. 5b). While the wave keeps breaking, higher frequency peaks are generated in the roller region (phases 2 in Fig. 5b). These peaks appear as alternately positive and negative gradient stripes close to the wave crest which exhibit nearly regular patterns both in time and space. Fig. 6a illustrates further this phenomenon with the example of a wave profile evolution.

To estimate the break point location of a tracked wave, the surface elevation spatial gradients at every point in the wave profile between the wave crest and an elevation $0.8H$ below the crest on the wave front face are extracted. This process is performed at every cross-shore position, at the moment when the wave crest passes that position (see example in Fig. 6a). The variance of these spatial gradients is then computed and used as a proxy for the break point detection: the variance increases considerably at the breaking onset, and remains much higher than when shoaling due to the roller activity (see example in Fig. 6b). Note that the

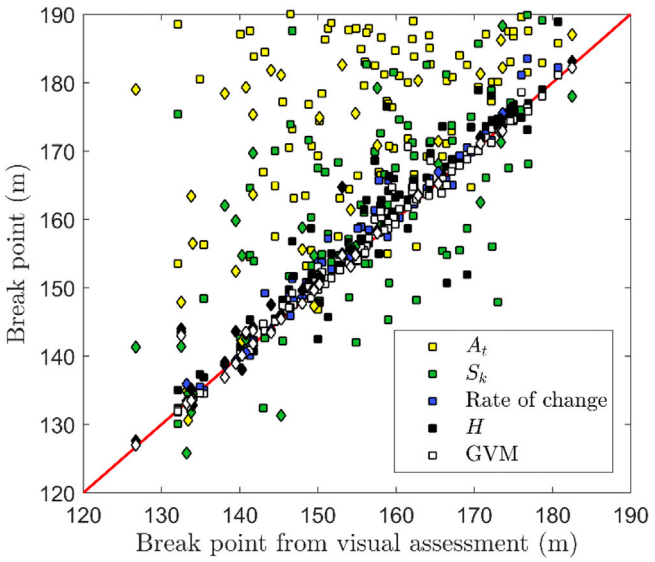


**Fig. 7.** Scatter plot of the different methods for the break point assessment. For a subset of 116 manually picked individual waves, the detected break point from each method is shown against the ground truth method (visual assessment from LiDAR data animations). Data from the 09/04 and 10/04 (plunging and spilling breaker types) are shown as squares while the rest of the data (predominantly spilling breakers) are represented using diamonds. (For interpretation of the references to colour in this figure legend, the reader is referred to the web version of this article.)

variance of the gradients is calculated only to 0.8H below the crest because when tracking waves individually, the wave trough - defined as minimum reached between two wave crests - can be relatively distant from the subsequent crest due to the presence of higher frequency waves. The first cross-shore location where the surface elevation gradients variance reaches the empirical threshold of 0.2 defines the break point.

## 4. Results

### 4.1. Performance of the break point detection methods

The different methods to assess the break point outlined in Section 3 were compared in terms of performance against the ground truth method for 116 individual waves from the 08/04, 09/04, 10/04 and 11/04 to cover the range of wave conditions experienced during the experiments. Fig. 7 shows a scatter plot of the estimated break point locations using all methods. From their fit to the 1:1 line, it is evident that for the chosen ground truth method, three methods stand out: GVM, the velocity-based (using a threshold of 6 m/s) and $H$-based methods. GVM provide the best fit with the smallest *RMSE* when compared to the ground truth method (1.75 m), followed by the method based on the rate of change of surface elevation and the $H$-based method with *RMSE* of 2.44 m and 4.52 m respectively.

The $S_k$-based and $A_t$-based methods provide the least accurate estimates of the break point, with *RMSE* of 13.62 and 22.52 m respectively. Although these two methods give different *RMSE*, the standard deviation is high and of the same order (around 13 m). The reason is that the $S_k$-based method often predicts a breakpoint seaward of the visually observed location, whereas the individual time asymmetry becomes minimal only at the break point or after during the bore propagation, meaning that the $A_t$-based method almost never predicts the break point earlier than it actually occurs. An example of this can be seen in Fig. 6d, where $A_t$ decreases until breaking ($x = 152.7$ m), but reaches its minimum value farther landward ($x = 158$ m). In other cases, this can be even farther landward in the inner surf, as developed bores can be steep, and their asymmetry small, as suggested by the presence of multiple small values in Fig. 6d. The absence of a defined peak at or near the break point for the $S_k$ parameter in part explains the discrepancies observed with the $S_k$-based method. Instead, the peak values in the cross-shore were often caused by the superposition of incident and reflected waves in either the shoaling or surf zones.

### 4.2. Sensitivity analysis of breaker detection methods

The sensitivity of GVM to the chosen threshold was investigated by performing the same analysis with two other thresholds of 0.15 and 0.3. With these two thresholds, *RMSE* of 2.16 and 4.69 m were obtained. The chosen value of 0.2 is therefore close to the optimal value for this ground truth method. The poorer performance obtained with the 0.3 threshold can be primarily explained by the time needed for the gradient variance to increase for spilling waves, tending to delay the detection of the break point.

The criterion for the method based on the rate of change of surface elevation was also examined. This parameter is expected to reach its maximum at the moment of breaking, however the presence of high-frequency peaks in the roller region generated during the breaking process not only leads to the good performance of the GVM, but also implies steep and rapidly-changing features in the front of the wave. When these changes are faster than those due to a steepening or breaking wave, the maximum rate of change in the wave path can therefore be located well away from the actual break point. This is illustrated in Fig. 6c, where multiple peaks are present after the break point, and the greatest peak does not correspond to the break point location. Similar to the $A_t$-based method, this criterion tends to predict the break point landward of its true location (Fig. 7). The choice of the upcrossing threshold method rather than the maximum location decreased the *RMSE* for this method from 6.61 m to 2.44 m. A drawback of this method lies in the lower rate of change observed for spilling waves. No break point could be detected for 9 of the 116 waves, because the surface elevation rate of change never exceeded the threshold. A more robust threshold accounting for the individual wave celerity is desirable (Longuet-Higgins and Smith, 1983), but at present, estimating the individual wave celerity based on a timeseries at a single point remains a challenge.

Although the maximum value of the wave height to water depth ratio $\gamma = H/h$ is sometimes used to define the break point, it was recently observed to increase in the inner surf zone, with the possibility of reaching higher values than at break point (Power et al., 2010). This parameter was also found to be affected by the presence of higher/lower frequency waves such as those reflected at high tide (Martins et al., 2017) or the formation of jets/splashes after breaking that can reach higher elevation than the crest itself at break point. A reduction in *RMSE* of 1.87 m to estimate the break point was obtained by using the maximum wave height $H$ rather than $\gamma$.

## 5. Concluding remarks

This paper reports on a field experiment undertaken in April 2016 at Saltburn-by-the-Sea, UK. Three 2D LiDAR scanners were deployed 20 m apart along the pier to obtain a complete surface elevation dataset throughout the surf and swash zones. A detailed field dataset of breaking waves was obtained, with data covering up to 100 m of the surf zone at a frequency of 25 Hz and a spatial resolution ranging from 0.02 to 0.25 m.

A new method to estimate the break point location from the detailed wave profile measurements is presented. It uses previously developed tracking algorithms and the high spatial and temporal resolution of the LiDAR dataset to assess the break point based on the variance of the surface elevation gradients in front of a tracked wave crest. Good ability to detect the break point location was obtained against a visual assessment of LiDAR data (*RMSE* = 1.75 m). Good performances were also obtained by the methods based on surface elevation rate of changes and on the wave height. The other methods based on geometrical considerations ($S_k$, $A_t$) tend to delay or detect the break point farther landward (Fig. 7). The error in break point location is mostly explained by the

increasing non-linearities in the wave shape after breaking.

Finally, the discrepancies observed in the break point location, and those found in the breaker parameters possibly explain the difficulty in obtaining simple relations between offshore wave parameters, beach slope and wave properties at the break point noted by Robertson et al. (2013). The ability to obtain high resolution data using a LiDAR and the analysis methods presented here may provide a good opportunity to make progress with this problem.

## Acknowledgements

The authors would like to acknowledge the financial assistance provided by the Engineering and Physical Sciences Research Council (EP/N019237/1). Kévin Martins was supported by the University of Bath, through a URS scholarship. The assistance of Perveen Mian and her colleagues at Redcar and Cleveland Council in facilitating access to the site is greatly appreciated. B. Bruder and J. Puleo were supported by SERDP (MR-2503) and the Unviersity of Delaware. We would also like to thank Aline Pieterse (University of Delaware, USA) for her assistance during the experiment.

## References

Adeyemo, M., 1968. Effect of beach slope and shoaling on wave asymmetry. Coast. Eng. Proc. 1 (11).

Almeida, L.P., Masselink, G., Russell, P., Davidson, M., 2015. Observations of gravel beach dynamics during high energy wave conditions using a laser scanner. Geomorphology 228, 15–27. http://dx.doi.org/10.1016/j.geomorph.2014.08.019.

Babanin, A., 2011. Breaking and Dissipation of Ocean Surface Waves. Cambridge University Press. http://dx.doi.org/10.1017/CBO9780511736162.

Birkemeier, W.A., Donoghue, C., Long, C.E., Hathaway, K.K., Baron, C.F., 1997. The 1990 DELILAH nearshore experiment: summary report. Tehcnical Report CHL-97-24. U. S. Army Waterw. Exp. Stn.

Blenkinsopp, C.E., Chaplin, J.R., 2007. Void fraction measurements in breaking waves, proceedings of the royal society of London a: mathematical. Phys. Eng. Sci. 463, 3151–3170. http://dx.doi.org/10.1098/rspa.2007.1901.

Blenkinsopp, C.E., Mole, M.A., Turner, I.L., Peirson, W.L., 2010. Measurements of the time-varying free-surface profile across the swash zone obtained using an industrial LiDAR. Coast. Eng. 57, 1059–1065. http://dx.doi.org/10.1016/j.coastaleng.2010.07.001.

Blenkinsopp, C.E., Turner, I.L., Allis, M.J., Peirson, W.L., Garden, L.E., 2012. Application of lidar technology for measurement of time-varying free-surface profiles in a laboratory wave flume. Coast. Eng. 68, 1–5. http://dx.doi.org/10.1016/j.coastaleng.2012.04.006.

Brodie, K.L., Raubenheimer, B., Elgar, S., Slocum, R.K., McNinch, J.E., 2015. Lidar and pressure measurements of inner-surfzone waves and setup. J. Atmos. Ocean. Technol. 32, 1945–1959. http://dx.doi.org/10.1175/JTECH-D-14-00222.1.

Carey, W.M., Fitzgerald, J.W., 1993. Low Frequency Noise from Breaking Waves, in: Natural Physical Sources of Underwater Sound: Sea Surface Sound (2). Springer, Netherlands, pp. 277–304.

Carini, R.J., Chickadel, C.C., Jessup, A.T., Thomson, J., 2015. Estimating wave energy dissipation in the surf zone using thermal infrared imagery. J. Geophys. Res. Oceans 120, 3937–3957. http://dx.doi.org/10.1002/2014JC010561.

Catalán, P.A., Haller, M.C., Plant, W.J., 2014. Microwave backscattering from surf zone waves. J. Geophys. Res. Oceans 119, 3098–3120. http://dx.doi.org/10.1002/2014JC009880.

Cowell, P.J., 1982. Breaker Stages and Surf Structure on Beaches, Coastal Studies Unit Technical Report No. 82/7 (Sydney, Australia).

Ebersole, B.A., Hughes, S.A., 1987. DUCK85 Photopole Field Experiment, ADA188477, DTIC Document.

Haller, M.C., Catalán, P.A., 2009. Remote sensing of wave roller lengths in the laboratory. J. Geophys. Res. Oceans 114. http://dx.doi.org/10.1029/2008JC005185.

Holman, R., Haller, M.C., 2013. Remote sensing of the nearshore. Annu. Rev. Mar. Sci. 5 (1), 95–113. http://dx.doi.org/10.1146/annurev-marine-121211-172408.

Longo, S., Petti, M., Losada, I.J., 2002. Turbulence in the swash and surf zones: a review. Coast. Eng. 45, 129–147. http://dx.doi.org/10.1016/S0378-3839(02)00031-5.

Longuet-Higgins, M.S., Smith, N.D., 1983. Measurement of breaking waves by a surface jump meter. J. Geophys. Res. Oceans 88, 9823–9831. http://dx.doi.org/10.1029/JC088iC14p09823.

Martins, K., Blenkinsopp, C.E., Zang, J., 2016. Monitoring individual wave characteristics in the inner surf with a 2-dimensional laser scanner (LiDAR). J. Sensors 2016, 1–11. http://dx.doi.org/10.1155/2016/7965431.

Martins, K., Blenkinsopp, C.E., Almar, R., Zang, J., 2017. The influence of swash-based reflection on surf zone hydrodynamics: a wave-by-wave approach. Coast. Eng. 122, 27–43. http://dx.doi.org/10.1016/j.coastaleng.2017.01.006.

Power, H.E., Hughes, M.G., Aagaard, T., Baldock, T.E., 2010. Nearshore wave height variation in unsaturated surf. J. Geophys. Res. 115, C08030 http://dx.doi.org/10.1029/2009JC005758.

Robertson, B., Hall, K., Richard, Z., Nistor, I., 2013. Breaking waves: review of characteristic relationships. Coast. Eng. J. 55, 1350002. http://dx.doi.org/10.1142/S0578563413500022.

Rosati, J.D., Gingerich, K.J., Kraus, N.C., 1990. SUPERDUCK Surf Zone Sand Transport Experiment, ADA225690, DTIC Document.

Senechal, N., Abadie, S., Gallagher, E., MacMahan, J., Masselink, G., Michallet, H., Reniers, A., Ruessink, G., Russell, P., Sous, D., Turner, I., Ardhuin, F., Bonneton, P., Bujan, S., Capo, S., Certain, R., Pedreros, R., Garlan, T., 2011. The ECORS-Truc Vert'08 nearshore field experiment: presentation of a three-dimensional morphologic system in a macro-tidal environment during consecutive extreme storm conditions. Ocean. Dyn. 61, 2073–2098. http://dx.doi.org/10.1007/s10236-011-0472-x.

Svendsen, I.A., 2006. Introduction to Nearshore Hydrodynamics, Advanced Series on Ocean Engineering. World Scientific.

Svendsen, I.A., Madsen, P., Buhr Hansen, J., 1976. Deformation up to breaking of periodic waves on a beach. Coast. Eng. Proc. 1 (15), 477–496.

Svendsen, I.A., Madsen, P., Buhr Hansen, J., 1978. Wave characteristics in the surf zone. Coast. Eng. Proc. 1 (16), 520–539. http://dx.doi.org/10.1061/9780872621909.031.